# An intriguing intermediate state as a bridge between antiferroelectric and ferroelectric perovskites

Hui Liu,[a] Zhengyang Zhou,[b] Yi Qiu,[b] Baotao Gao,[a] Shengdong Sun,[a] Kun Lin,[a] Lei Ding,[d] Qiang Li,[a] Yili Cao,[a] Yang Ren,[c] Junliang Sun,[b,*] Xianran Xing,[a] and Jun Chen[a,*]

[a]Beijing Advanced Innovation Center for Materials Genome Engineering, and School of Mathematics and Physics, University of Science and Technology Beijing, Beijing 100083, China

[b]BNLMS, College of Chemistry & Molecular Engineering, Peking University, Beijing 100871, China

[c]X-Ray Science Division, Advanced Photon Source, Argonne National Laboratory, Argonne, Illinois 60439, USA

[d]ISIS Facility, Rutherford Appleton Laboratory, Harwell Oxford, Didcot OX11 0QX, UK

*Corresponding author. junchen@ustb.edu.cn and junliang.sun@pku.edu.cn

## I. Sample preparation and macroscopic properties measurements

The $Pb_{0.99}Nb_{0.02}[(Zr_{0.57}Sn_{0.43})_{1-y}Ti_y]_{0.98}O_3$ ($y$ = 0.06, abbreviated as PNZST) ceramics were prepared by conventional solid-state method. Firstly, stoichiometric PbO (5% excess), $ZrO_2$, $SnO_2$, $TiO_2$, and $Nb_2O_5$ precursors with analytical purity were mixed. Then the mixture was calcined at 850 °C for 4 h. Part of calcined powder was pressed into pellets and then sintered at 1300 °C for 3 h covered with remaining powders to compensate the evaporation loss of PbO. The ceramics were polished and annealed at 400 °C to release stresses. For the *in-situ* high-energy diffraction (HE-SXRD) measurements, the bar-shape ceramic samples with dimensions of 6×1×0.6 $mm^3$ were cut, then the gold electrodes were deposited on the two sides of 6×1 $mm^2$ of the samples. The ceramic pellets were crushed into fine powder and annealed at 400 °C for 2 h to release residual stresses for the high-resolution synchrotron x-ray diffraction (HR-SXRD), and time-of-flight neutron powder diffraction (NPD) measurements. The macroscopic properties of polarization *vs* electric field (*P*-*E*) loops were measured by a ferroelectric tester (model aixACCT, TF Analyzer 1000) at a frequency of 1 Hz at room temperature. Powder SHG measurement was performed at room temperature on a modified Kurtz-NLO system using a pulsed Nd: YAG laser with an incident wavelength of 1064 nm.

## II. Diffraction measurements

**In-situ high-energy diffraction measurements (HE-SXRD).** *In-situ* HE-SXRD studies were performed at 11-ID-C at Advanced Photon Source (APS) at Argonne National Laboratory. The x-ray beam had a spot size of 300 μm × 300 μm, photon energy of about 110 keV and a wavelength of 0.11165 Å. Diffraction patterns were measured in forward scattering geometry on a Perkin Elmer amorphous silicon area detector placed approximately 1800 mm away from the sample. The electric field was applied from 0 kV/mm to 5 kV/mm with a step of about 0.5 kV/mm. The direction of the electric field was perpendicular to the beam line (Fig. S1). As shown in Fig S1, the direction parallel to the electric field was defined as $\varphi = 0°$, perpendicular to the electric field as $\varphi = 90°$. The data of Debye rings were divided into equidistant sectors at 15° intervals to integrate the diffraction intensities. The sample of ceria standard was used to calibrate the related parameters of detector. The one-dimensional diffraction intensity *vs.* $2\theta$ patterns data integration was performed by the Fit2d software. One-dimensional XRD patterns

were transformed into intensity as a function of $Q$, which can be written as $Q = 4\pi sin\theta/\lambda$. Due to the negligible preferential effect at 45° sector, at which the diffraction patterns can be used to structure refinements.

**High resolution synchrotron x-ray diffraction measurements.** High resolution synchrotron x-ray diffraction were measured at BL44B2 beamline of SPring-8 with Debye-Scherrer camera ($\lambda$ = 1.08 Å), which presents state-of-the-art angular resolution for powder diffraction measurements [1]. The powder samples were placed in a 0.1 mm diameter Lindemann glass capillary that was spun during the experiments.

**Time-of-flight neutron powder diffraction (NPD) measurements.** The neutron powder diffraction were conducted at the ISIS pulsed neutron and muon facility of the Rutherford Appleton Laboratory, on the WISH diffractometer.

**3D electron diffraction (ED) experiments.** For 3D ED experiments, a pellet specimen was pretreated with ion beam thinning. The 3D ED data were collected by rotation electron diffraction method, which was processed on a JEOL-2100 electron microscope with an operation voltage of 200 kV (Fig. S3).

## III. Details of structure analysis

The detailed crystal structure was refined based on the Rietveld method performed on the software Jana2006 [2]. Background parameters, scale factor, zero correction, pseudo-Voigt function profile parameters, unit cell parameters, atomic coordinates, isotropic thermal parameters, and positional modulation parameters were refined.

According to the reflection conditions of the main reflections, the pseudo-tetragonal symmetry can be primarily confirmed. Based on the presence of $½\{ooo\}_p$ satellite reflections, the antiphase oxygen octahedral tilting can be confirmed in the average structure. Besides, the space group should be an acentric symmetry with polar structure because PNZST exhibits non-zero remnant polarization and SHG effect. Therefore, the average structure firstly can be assigned as a polar pseudo-tetragonal with antiphase octahedral tilting. According to Glazer's tilt notation of the superposition with antiphase tilting, the plausible structures can be *I*4*cm*, *Ima*2, *Imm*2. For the

lower symmetry systems of monoclinic and triclinic are not considered. Subsequently, based on the 3D electron diffraction data, the structure is determined as *Ima*2 with $a^-a^-c^0$ tilting configuration [3]. In order to compare with the structure of $PbZrO_3$, the polarization axis is set in $b_o$ axis. Hence, the structure can be transformed into *Ic*2*m*. Based on the thermal expansion behavior obtained by the LeBail fitting, that the nearly linear large positive thermal expansion behavior the $c_o$ axis, while the nonlinear trends, and low thermal expansion behavior for $a_o$ and $b_o$ axis, the polarization should be within the $a_o$-$b_o$ plane according the spontaneous volume ferroelectrostriction effect [4].

According to symmetry operators, the incommensurate modulation vector $\boldsymbol{q} \approx 0.138(\boldsymbol{a}_p^* + \boldsymbol{b}_p^*)$ obtained by the SAED can be transformed into $\boldsymbol{q} = 0.2765\boldsymbol{a}_o^*$ in orthorhombic symmetry. The results of the joint full-profile Rietveld refinement against HR-SXRD and NPD show that the periodicity in the (3+1)D superspace group can be determined as *Ic*2*m*($\alpha$00)000 ($a$ = 5.8139(2) Å, $b$ = 5.8141(2) Å, $c$ = 8.1705(1) Å, $\alpha$ = 0.2765(1)).

In the (3+1)D superspace group, each parameter of the modulated structure can be expanded as a Fourier series,

$$p^{\mu}(x_4) = \sum_m \left[p_{sm}^{u}(sin2\pi x_4) + p_{cm}^{u}(cos2\pi x_4)\right]$$

where $x_4 = q_1^{ru} + t$, and $t$ is internal phases.

## IV. Details of calculation of polar displacements

Based on the obtained structure parameters and detailed atomic position information after refinements, the polar displacements can be calculated. In perovskite oxides ($ABO_3$), the polar displacements including $A$ site and $B$ site polar displacements. The $A$ site displacement is the displacement between $A$ cation and the centroid of the oxygen polyhedron in the $AO_{12}$ polyhedron, and the $B$ site displacement is the displacement between the $B$ cation and the centroid of the oxygen octahedron in the $BO_6$ octahedron.

## V. Supporting Figures and Tables

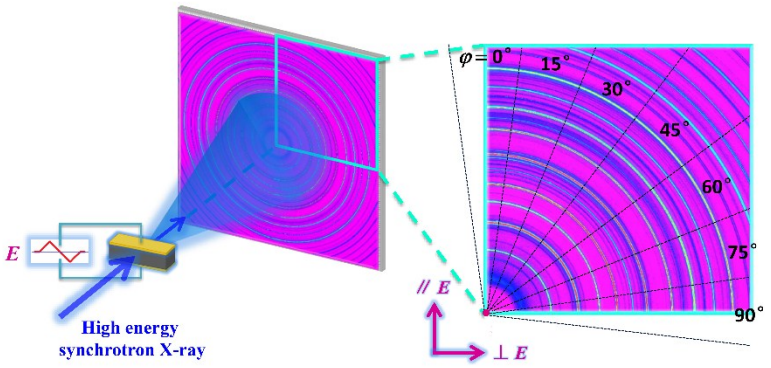


Fig. S1. Schematic of in-situ high-energy synchrotron X-ray diffraction experiments.

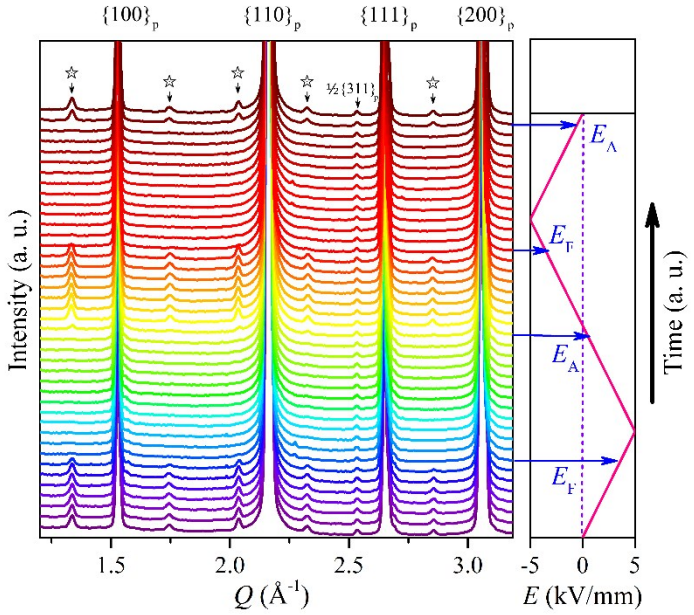


Fig. S2. Evolution of satellite peaks with bipolar electric field at 45° sector of PNZST. The incommensurate peaks are marked with asterisks. The in-situ SXRD experiments were performed on the beamline 11-ID-C at Advanced Photon Source (APS) at Agronne National Laboratory.

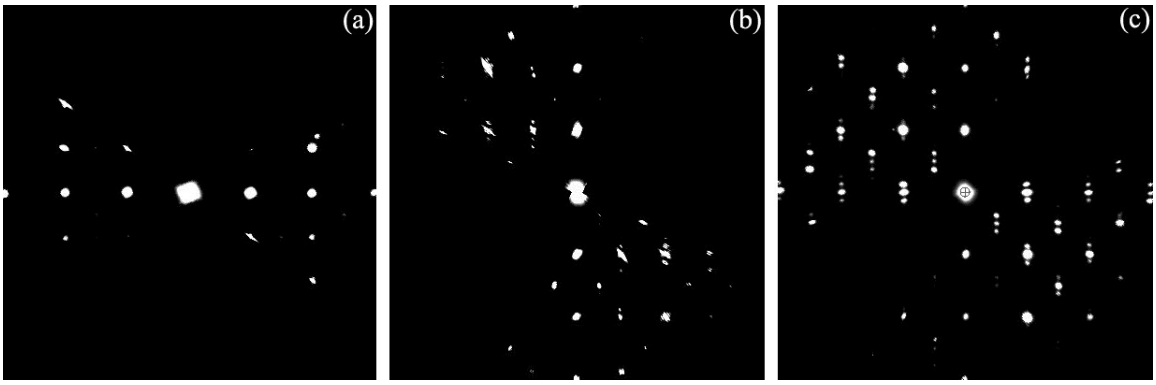


Fig. S3. 3D electron diffraction data. Selected planes in the reciprocal lattice corresponding to the (a) $(h0l)_o$, (b) $(hk0)_o$, and (c) $(0kl)_o$ planes.

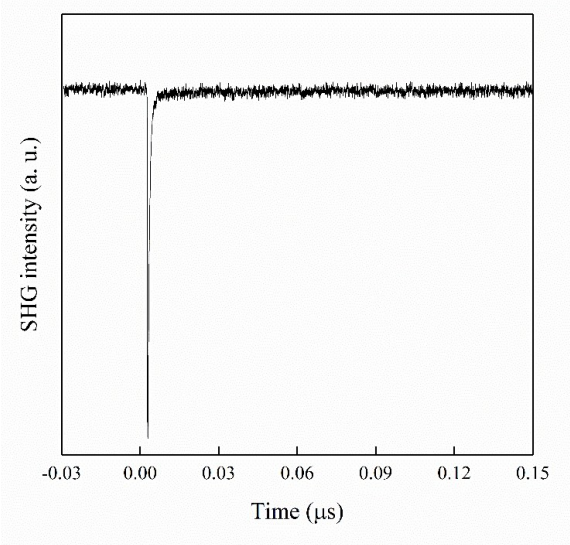


Fig. S4. The powder SHG responses of PNZST powder measured at RT.

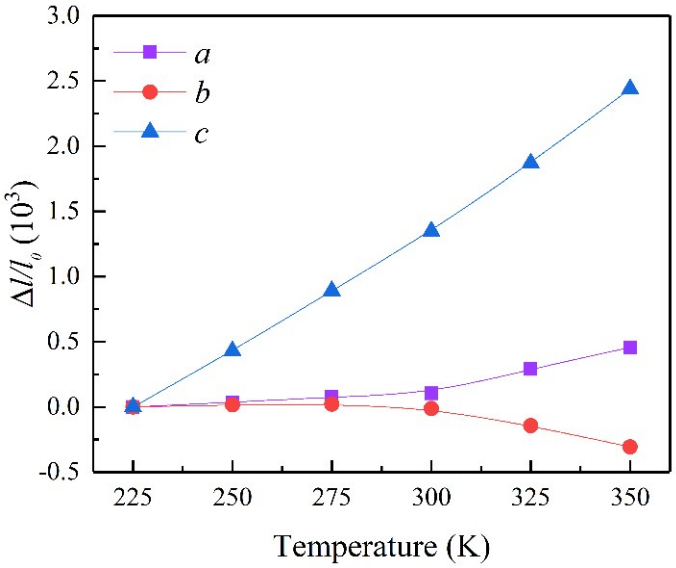


Fig. S5. Thermal expansion behavior obtained by LeBail fitting of the temperature dependent HR-SXRD data of PNZST.

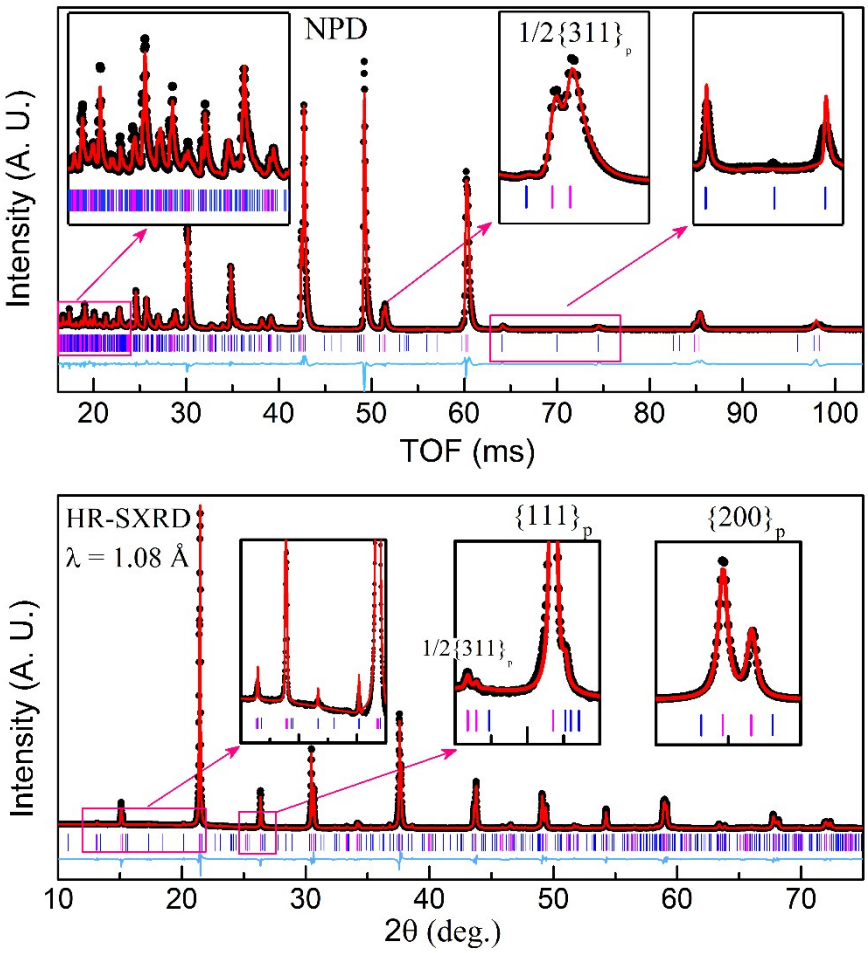


Fig. S6. Full-profile Rietveld refinement of PNZST. The observed (black points), the calculated (red line) and the differences (light blue line) are depicted. The thick marks indicate the Bragg peak positions (blue ones indicate incommensurate Bragg peak positions). It needs to be noted that these observed weak satellite reflections at high *d* ranges present border FWHM than the calculated one. These reasons would cause it. One is that the real crystal structure of PNZST does not have the perfect periodicity due to the existence of domain wall and defect. Furthermore, there are some limitations in the present structure refinement method for modulated structures. For example, the same profile function of the satellite and main reflections is set during the refinement.

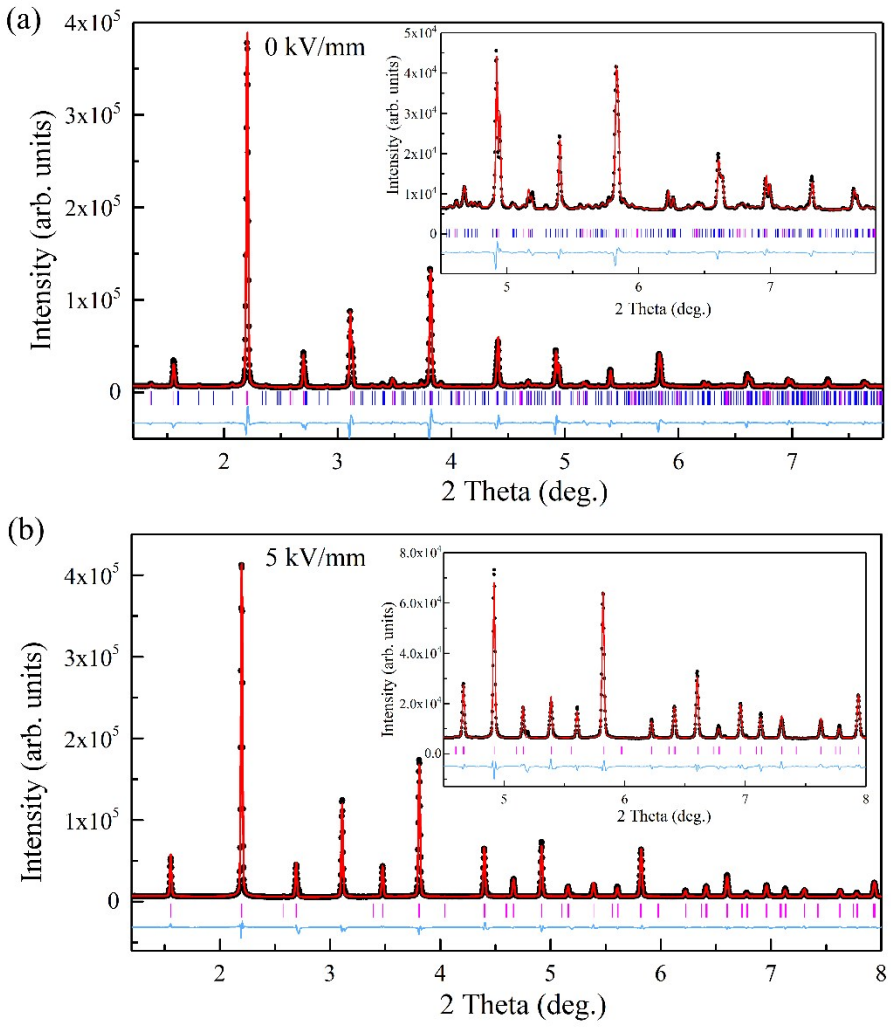


Fig. S7. The comparison of the observed (black points) and the calculated (red line) diffraction patterns of PNZST. The light blue line at the bottom indicates the difference. The thick marks indicate the Bragg peak positions (blue ones for incommensurate Bragg peak positions). (a) 0 kV/mm, and (b) 5 kV/mm. The in-situ SXRD experiments were performed on the beamline 11-ID-C at Advanced Photon Source (APS) at Argonne National Laboratory.

Table S1. (3+1)D incommensurately modulated structure parameters of PNZST at 0 kV/mm.

| Space group $Ic2m(\alpha 00)$ | $a$ = 5.8139(2) Å, $b$ = 5.8141(2) Å, $c$ = 8.1705(1) Å<br>$\alpha$ = 0.2765(1), $V_p$ = 69.045 Å$^3$ | | | | |
|---|---|---|---|---|---|
| Atom | $x$ | $y$ | $z$ | $U_{iso}$ | $Occ.$ |
| Pb | 0.5023(2) | 0.0222(10) | 0.25 | | |
| sin1 | -0.0024(1) | 0.0033(1) | 0 | 0.0367(1) | 1 |
| cos1 | -0.0072(7) | -0.0314(3) | 0 | | |
| Zr/Sn/Ti/Nb | 0 | 0.0074(20) | 0 | | |
| sin1 | 0.0035(5) | 0 | -0.0007(1) | 0.02623(0) | 1 |
| cos1 | 0 | -0.0081(12) | 0 | | |
| O1 | 0.7584(5) | 0.2732(6) | 0.0236(1) | | |
| sin1 | 0.0026(10) | -0.0078(10) | -0.0056(3) | 0.02937(2) | 1 |
| cos1 | 0.0092(5) | 0.0217(4) | -0.0044(7) | | |
| O2 | 0.5023(2) | 0.0333(8) | 0.25 | | |
| sin1 | -0.0024(1) | 0.0169(8) | 0 | 0.02937(2) | 1 |
| cos1 | -0.0072(7) | 0.0280(6) | 0 | | |
| $R_p$ = 4.5%, $R_{wp}$ = 6.2%, $\chi^2$= 7.5 | | | | | |

Table S2. The structure parameters of PNZST at 5 kV/mm.

| Space group $R3c$ (H) | $a = b$ = 5.8126(2) Å, $c$ = 14.2675(1) Å<br>$V_p$ = 69.579 Å$^3$ | | | | |
|---|---|---|---|---|---|
| Atom | $x$ | $y$ | $z$ | $U_{iso}$ | $Occ.$ |
| Pb | 0 | 0 | 0.2794(1) | 0.0190(2) | 1 |
| Zr/Sn/Ti/Nb | 0 | 0 | 0.1076(0) | 0.0083(0) | 1 |
| O | 0.2101(23) | 0.3513(21) | 0.0833 | 0.0162(5) | 1 |
| $R_p$ = 3.0%, $R_{wp}$ = 5.3%, $\chi^2$= 5.2 | | | | | |

Table S3. The calculated polar displacement of modulated AFE (0 kV/mm) and FE (5 kV/mm) of PNZST.

| **Modulated AFE of PNZST at 0 kV/mm** | | | | |
|---|---|---|---|---|
| N | Polar displacement (pm) | | | |
| | $[\bar{1}10]_p$ | | $[110]_p$ | |
| | *A* site | *B* site | *A* site | *B* site |
| 0 | 0.14 | -3.65 | 17.65 | 21.07 |
| 0.5 | 6.17 | 3.95 | -4.25 | 12.94 |
| 1 | 7.72 | 8.68 | -21.25 | 3.77 |
| 1.5 | 4.11 | 7.44 | -21.68 | 0.21 |
| 2 | -2.57 | 0.96 | -5.30 | 4.31 |
| 2.5 | -7.39 | -6.23 | 16.74 | 13.65 |
| 3 | -6.85 | -8.89 | 28.47 | 21.44 |
| 3.5 | -1.34 | -5.11 | 21.37 | 22.04 |
| 4 | 5.14 | 2.38 | 0.60 | 15.01 |
| 4.5 | 7.88 | 7.90 | -17.79 | 6.07 |
| 5 | 5.30 | 8.23 | -23.10 | 0.41 |
| 5.5 | -1.13 | 2.60 | -9.84 | 2.81 |
| 6 | -6.74 | -4.92 | 12.38 | 11.53 |
| 6.5 | -7.46 | -8.87 | 27.45 | 20.25 |
| 7 | -2.77 | -6.39 | 24.43 | 22.64 |
| **FE of PNZST at 5 kV/mm** | | | | |
| | Polar displacement (pm) | | | |
| | $[111]_p$ | | | |
| | *A* site | | *B* site | |
| | 40 | | 14 | |

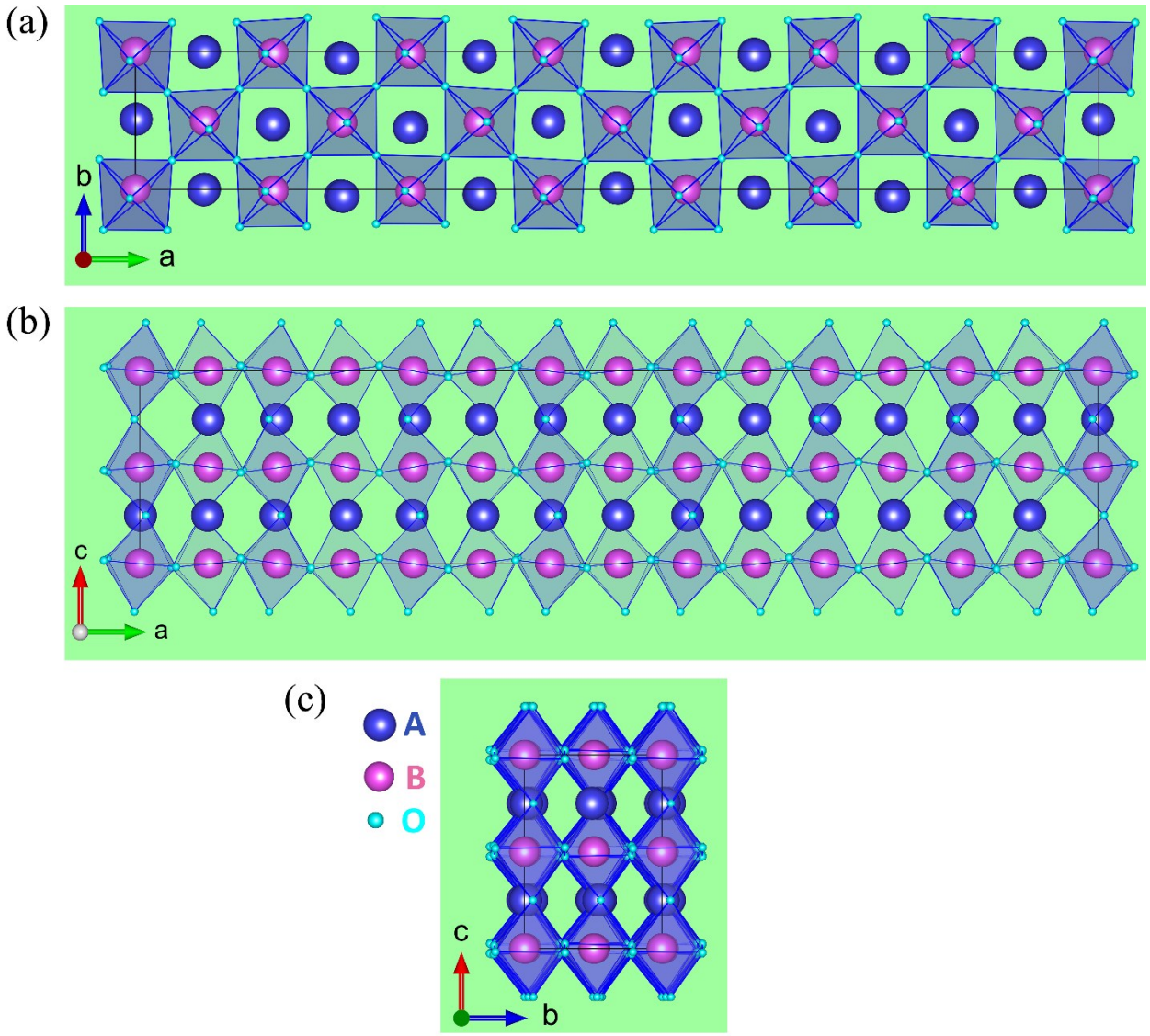


Fig. S9. The superstructure of PNZST at zero electric field with $7a_o \times 1b_o \times 1c_o$ modulated approximant along (a) *c* axis, (b) *b* axis and (c) *a* axis. The A indicates Pb atom, and B indicates Nb, Zr, Sn and Ti atom.

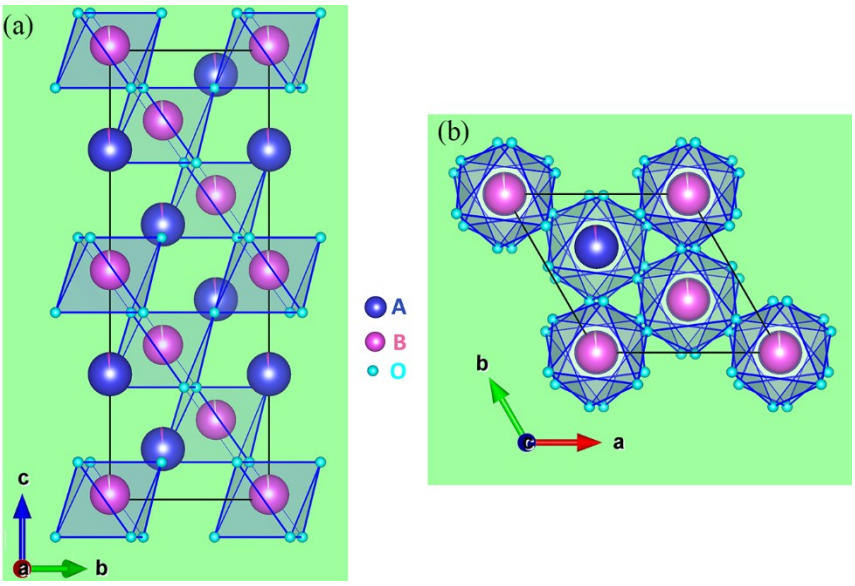


Fig. S10. The structure ferroelectric phase of PNZST at 5 kV/mm. (a) a axis, and (b) c axis. The A indicates Pb atom, and B indicates Nb, Zr, Sn and Ti atom.

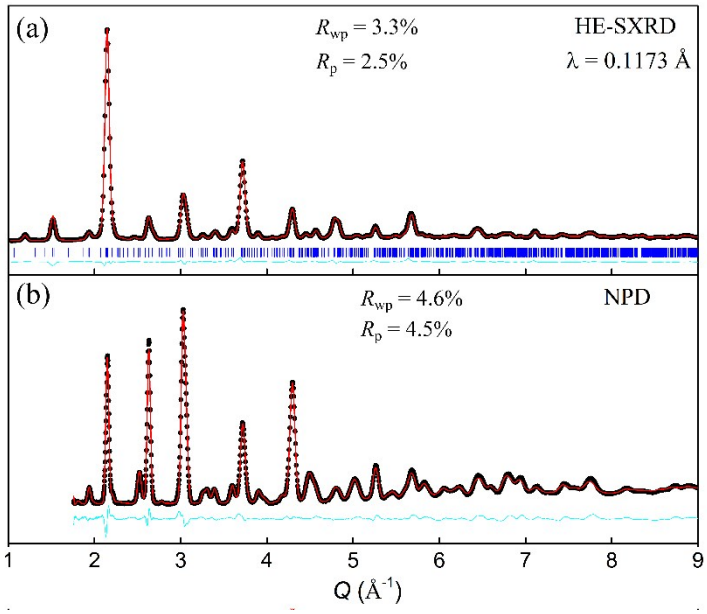


Fig. S11. Full-profile Rietveld refinement of $PbZrO_3$. The observed (black points), the calculated (red line) and the differences (light blue line) are depicted. The thick marks indicate the Bragg peak positions.

Table. S4. The structure parameters of $PbZrO_3$ at room temperature.

| Space group *Pbam* | $a$ = 5.8821(2) Å, $b$ =11.7730(3) Å, $b$ =8.2461(2) Å $\alpha = \beta = \gamma = 90°$ | | | | |
|---|---|---|---|---|---|
| | atom position | | | $U_{iso}$ | Occ. |
| | $x$ | $y$ | $z$ | | |
| Pb1 | 0.7111(13) | 0.1300(6) | 0 | 0.0202 | 1 |
| Pb2 | 0.70653(12) | 0.1257(5) | 0.5 | 0.0202 | 1 |
| Zr | 0.24252(6) | 0.1213(5) | 0.2503(10) | 0.0075 | 1 |
| O1 | 0.3004(15) | 0.1012(9) | 0 | 0.0139 | 1 |
| O2 | 0.2654(9) | 0.1562(4) | 0.5 | 0.0139 | 1 |
| O3 | 0.0251(8) | 0.26005 | 0.2254(8) | 0.0139 | 1 |
| O4 | 0 | 0.5 | 0.2919(10) | 0.0139 | 1 |
| O5 | 0 | 0 | 0.2716(14) | 0.0139 | 1 |

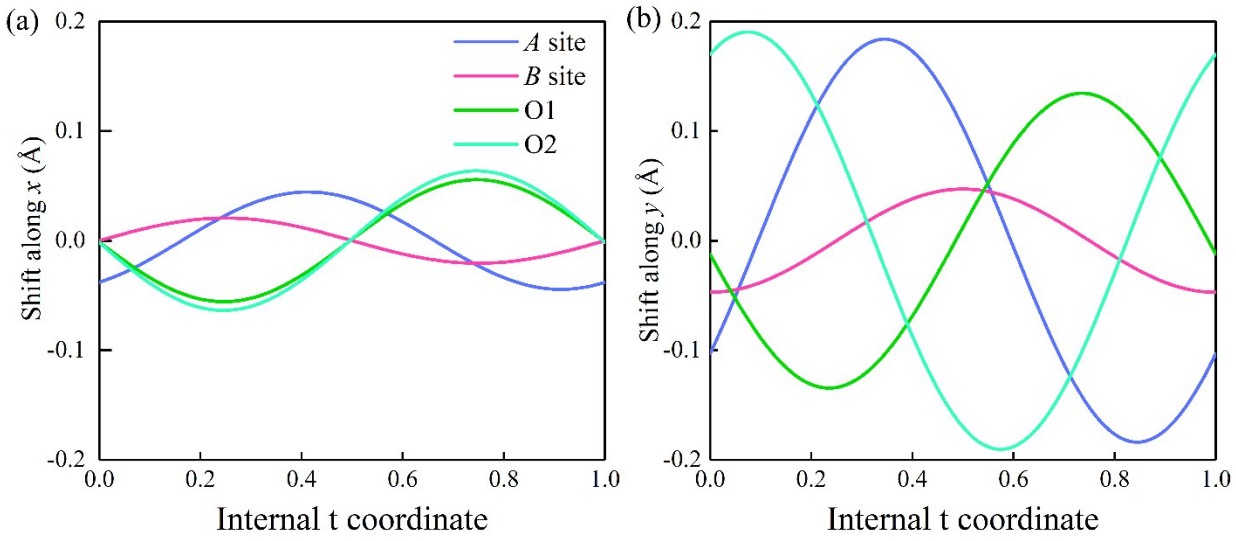


Fig. S12. Deviations of the *A* site, *B* site and O atoms from their average positions of PNZST as a function of the internal *t* coordinate, (a) along *a* axis (*x*) and (b) along *b* axis (*y*).

[1] K. Kato, R. Hirose, M. Takemoto, S. Ha, J. Kim, M. Higuchi, R. Matsuda, S. Kitagawa, and M. Takata, AIP Conf. Proc. **1234**, 875 (2010).

[2] V. Petricek, M. Dusek, and L. Palatinus, Z. Kristallogr. **229**, 345 (2014).

[3] A. M. Glazer, Acta Crystallogr. Sect. B **28**, 3384 (1972).

[4] J. Chen, L. Hu, J. Deng, and X. R. Xing, Chem. Soc. Rev. **44**, 3522 (2015).